Research Square

Preprints are preliminary reports that have not undergone peer review.
They should not be considered conclusive, used to inform clinical practice,
or referenced by the media as validated information.

Microstructure evolution and mechanical properties of AA6061/AA1100/AA6061 dissimilar aluminum alloy fabricated by friction stir additive manufacturing

Yuqiang Han
Suzhou University of Technology
Peifeng Wu
Suzhou University of Technology
Chunfa Lin
chunfalin1852@szut.edu.cn
Suzhou University of Technology
Sichang Zhang
Suzhou University of Technology
Yaocheng Zhang
Suzhou University of Technology
Enhao Wang
Harbin University of Science and Technology

Research Article

Keywords: Dissimilar aluminium alloy, Friction stir additive manufacturing, Microstructure evolution, Mechanical properties

Posted Date: March 12th, 2026

DOI: https://doi.org/10.21203/rs.3.rs-8589146/v1

License: This work is licensed under a Creative Commons Attribution 4.0 International License.
Read Full License

Microstructure evolution and mechanical properties of AA6061/AA1100/AA6061 dissimilar aluminum alloy fabricated by friction stir additive manufacturing

Yuqiang Han[a], Peifeng Wu[a], Chunfa Lin[a,*], Sichang Zhang[a], Yaocheng Zhang[a,**], Enhao Wang[b,***]

[a] School of Automotive Engineering, Suzhou University of Technology, Changshu, 215500, China

[b] School of Materials Science and Chemical Engineering, Harbin University of Science and Technology, Harbin,150080, China

*Corresponding author: chunfalin1852@szut.edu.cn, +86-18262102784

**Corresponding author:zhangyc@szut.edu.cn, +86-13962489676

***Corresponding author: enhaowang@hrbeu.edu.cn, +86-15245088956

Abstract

In this study, a dissimilar aluminum alloy build of AA6061/AA1100/AA6061 was successfully fabricated using friction stir additive manufacturing (FSAM) process. Through systematic characterization, the materials flow, mixing features and microstructure evolution across specific regions along the build depth were investigated. Additionally, mechanical properties and fracture behavior of the final build were also explored. The results revealed that equiaxed grains with average grain sizes ranging from 4.9 μm to 10.5 μm were formed in central regions of each additive layers. In addition, the average grain sizes of thermal mechanical affected zones below the stir zones decreased significantly to 2.6~2.7 μm, primarily due to the subgrain refinement mechanism. Texture analysis showed a dominant presence of deformed and shear textures throughout all regions, owing to adequate shear strain suffering from tool. The major precipitates presented in stir zones consisted of Al_8Fe_2Si, β and β'. Furthermore, the FSAM build showed remarkable drops in yield strength (101.3 MPa) and ultimate tensile strength (213.0 MPa), compared to AA6061-T6 base metal. Moreover, microhardness fluctuation along the build depth were observed, owing to the variation of dislocation densities and grain orientations. These findings offer the academic foundation for further development of FSAM in producing dissimilar alloy build and promote their industrial applications.

Key words: Dissimilar aluminium alloy; Friction stir additive manufacturing; Microstructure

evolution; Mechanical properties

1. Introduction

Aluminum alloy has low density, high specific strength, and superior corrosion resistance, which is widely applied in aerospace and automotive manufacturing sectors [1,2]. With the global trend toward lightweight transportation, the demand of larger-scale aluminum alloy structural components have been increasing [3,4]. Additive manufacturing (AM) is a well-established advanced technique using metal powder or wire as raw materials to create 3D objects with unrestricted shape and dimension. It involves the addition of materials layer by layer through melting and solidification processes, which exhibits inherent advantages including cost-effectiveness, accelerated production cycles and exceptional design adaptability [5,6]. However, fusion-based additive manufacturing techniques, such as laser powder bed fusion (LPBF) and wire arc directed energy deposition (WA-DED), often introduce defects like porosity, cracks and grain coarsening during the liquid-to-solid transformation of aluminum alloy builds [7-10]. To solve these defects and enhance the mechanical properties of the fabricated components, it is necessary to explore a more suitable AM technique for aluminum alloys.

Friction stir additive manufacturing (FSAM), an emerging solid-state additive manufacturing (AM) technique, has demonstrated significant potential for producing lightweight metal components, particularly aluminum alloy [11,12]. By eliminating the melting process, FSAM effectively reduces common defects such as porosity, cracks and grain coarsening that are often encountered in fusion-based AM techniques [13,14]. FSAM technique operates based on the principles of friction stir lap welding (FSLW), utilizing a non-consumable rotating tool with a pin and shoulder to sequentially bond individual sheets, thereby constructing a multilayered component [15,16]. During FSAM, the tool is inserted into the upper surface of the stacked sheets and moves in the desired direction, generating frictional heat and inducing severe plastic deformation at the interfaces to achieve robust bonding. Notably, the geometric features of the rotating tool, including the dimensions of the pin and shoulder, as well as the pin configuration, play a critical role in determining the quality of the build [17]. Palanivel et al. [18,19] investigated the microstructure characteristics and mechanical properties of WE43 alloy and AA5083 alloy builds prepared using FSAM.

They reported that variations in grain refinement were found within the stir zone of the build owing to different strain rates and temperature across various additive layers during FSAM process. The mechanical properties of the FSAM build were significantly enhanced compared to those of base metals. Mao et al. [20] used AA7075 alloys to fabricate a multilayered FSAM build and explored its local mechanical properties in detail. Their results indicated that the entire build achieved a tensile strength of 240~270 MPa, surpassing that of the aluminum base metal. Additionally, the top region of the build exhibited the maximum tensile strength attributing to fine grains and desired precipitate characteristics. Similar trends in mechanical property improvement from the bottom to the top of the FSAM build were reported by Zhao et al. [21] for 2195 Al-Li alloys, further highlighting the influence of process dynamics on material performance. He et al. [22] conducted a study on the microstructure evolution and mechanical properties of Al-Zn-Mg alloy along the FSAM building direction. They found that grain growth and precipitates coarsening were occurred in bottom region of the build owing to multi-pass thermal cycles during FSAM, which led to the decreases in microhardness and tensile strength of the build compared to base metal. Jiang et al. [23] adopted different rotational and translational speeds to fabricate 2060 Al-Li alloy build and investigated the influence of process parameters on microstructure and mechanical properties of the build. They discovered that finer equiaxed grains (2~5 μm) were formed in the stir zones and the microhardness reached a maximum of 135 HV at rotational speed of 1600 r/min and translational speed of 300 mm/min due to lower heat accumulation. Li et al. [24] further advanced the understanding of FSAM by employing an underwater FSAM technique to fabricate Al-Zn-Mg-Cu alloy builds. Their comprehensive characterization of the microstructure and mechanical behavior demonstrated that the presence of cooling water significantly reduced the thermal cycling effect, leading to a substantial decrease in the average grain size of the build, particularly in the bottom region (0.8 μm). These findings underscore the importance of adjusting process parameters and cooling modes to control and optimize the microstructure and mechanical properties of the build.

Previous studies have demonstrated the practical potential of FSAM in producing lightweight and high-performance structural components, particularly for aluminum alloys. While current research predominantly focuses on FSAM of similar aluminum alloy systems,

with extensive investigation into the relationship between process parameters and build quality, the application of FSAM to dissimilar aluminum alloy combinations has been limited, and the associated process mechanisms remain poorly understood. Therefore, in this study, we employ the FSAM process to fabricate a AA6061/AA1100/AA6061 dissimilar aluminum alloy build, and offers a comprehensive analysis of material intermixing behavior, microstructure evolution and mechanical properties of the additive regions. The results will provide a theoretical basis of FSAM for dissimilar alloys and promote the application of FSAM technique in practice.

2. Experimental details

2.1 Materials and methods

AA6061-T6 and AA1100-H14 aluminum alloy sheets (dimensions: 150 mm × 75 mm × 2 mm) were used as base metals in the current work. Their chemical compositions are listed in Table 1. Prior to FSAM, all alloy sheets were pretreated through mechanical grinding using abrasive paper to remove surface oxidation and grease. Subsequently, the surfaces were subjected to ethanol cleaning and immediate drying to eliminate residual impurities.

The multi-layered fabrication was carried out using a GWM-850 friction stir welding system (Jiangsu Dongheng Group High-tech Industry Co., Ltd). A stir tool fabricated from H13 steel, featuring a cylinder-shaped shoulder and a tapered cylindrical threaded pin, was employed for FSAM process. The shoulder had a diameter of 22 mm, and the pin root and tip diameters were 8 mm and 6 mm, respectively. Notably, circumferential grooves were machined on the bottom surface of shoulder in order to promote plastic flow and convergence of materials during FSAM process. Considering the sheet thickness of 2 mm, the pin length was set to 3.5 mm, allowing the pin to penetrate from the top sheet to the mid-thickness of the bottom sheet. This design was beneficial to improve interfacial bonding quality via the synergistic effects of re-stirring and reheating. Fig. 1a shows a photograph of the stir tool along with a corresponding schematic of its geometric dimensions. FSAM was performed with a tool rotation speed of 1100 r/min, a traverse speed of 120 mm/min, a tilt angle of 0°, and a plunge depth of 0.2 mm. All passes were manufactured in the same travel direction. These parameters were selected through preliminary trials aimed at optimizing plastic material flow and minimizing internal defects in the build. The final configuration consisted

of a three-layer laminate: AA6061 sheets as the top and bottom layers and an AA1100 sheet in the middle. For simplicity, the build is designated as 616 FSAM given the grading initials of individual aluminium alloy layers. Fig. 1b presents the schematic diagram of the FSAM process. It is necessary to point out that flash formation was observed on the upper surface of the build after each FSAM pass. To ensure proper surface contact for subsequent layer addition, these flash edges were removed using an angle grinder.

Table 1 The chemical composition (wt.%) of aluminium alloy sheets used in this study.

Materials	Mg	Si	Fe	Cu	Zn	Cr	Mn	Ti	Al
AA6061-T6	1.01	0.62	0.37	0.24	0.12	0.11	0.11	0.02	Bal.
AA1100-H14	-	0.30	0.35	0.02	0.08	-	0.03	-	Bal.

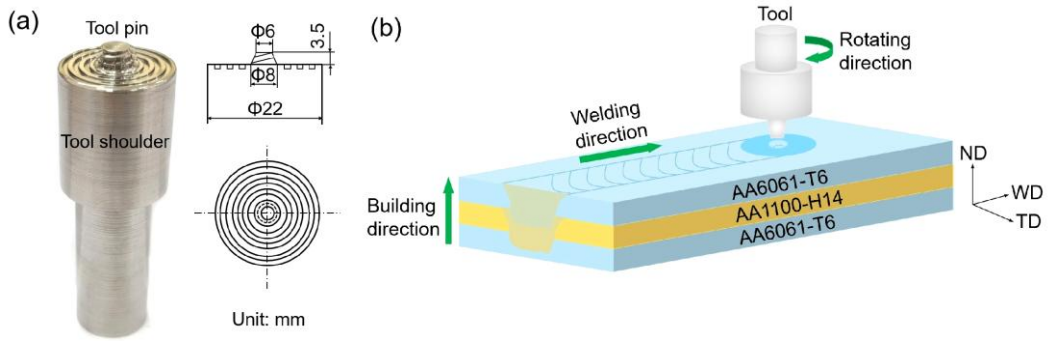


Fig. 1 Photography and dimensions of stir tool (a) and schematic diagram of FSAM process (b).

2.2 Microstructural Characterization

For microstructural analysis, samples were sectioned perpendicular to the welding direction (WD), followed by standard metallographic preparation, including sequential grinding with silicon carbide abrasive papers and polishing with diamond suspensions of decreasing particle size. Subsequently, the polished surfaces were etched with Weck's reagent (4 g $KMnO_4$, 1 g NaOH and 100 ml H_2O) for 12 s, and then wiped with 25% (v/v) nitric acid in ethanol to ensure optimal microstructural contrast. The materials flow and mixing features in stir zones of the FSAM build were observed by optical microscope (OM, Vert.A1 Zeiss) and scanning electron microscopy (SEM, Regulus 8100 Hitachi). To assess the recrystallization behavior, dislocation density, and texture components in different regions of the build, electron backscatter diffraction (EBSD) analysis was conducted using a Gemini SEM 500 (Zeiss) equipped with a corresponding detector. The samples for EBSD analysis were electro-polished in an ethanol solution containing 8% (v/v) perchloric acid at room

temperature with 15 V for 15 s. The EBSD data were further processed and analyzed via HKL Channel 5 software. Furthermore, the morphology and composition of precipitated phases within stir zones of the build were examined by transmission electron microscope (TEM, Talos F200X, FEI). TEM samples were prepared through the method of grinding and ion-beam thinning.

2.3 Mechanical testing

To evaluate the mechanical properties of the 616 FSAM build, tensile tests were conducted at a strain rate of 0.001/s using an UTM5305 electronic universal testing machine (Shenzhen Suns Technology Stock Co., Ltd) at room temperature. Tensile samples were extracted from the mid-region of the build along the WD. The geometry of the tensile samples is achieved by ASTM E8/E8M-16a standard, as depicted in Fig. 2a. During the tensile testing, an extensometer was used to monitor the deformation of the sample. In addition, the gauge length elongation of each sample was measured for calibration. For comparative purposes, tensile tests were also performed on the base metals under identical testing conditions. To minimize the influence of surface irregularities and potential stress concentrations, all samples were mechanically polished prior to testing. Following the tests, the fracture surfaces were observed by SEM to study the fracture mechanisms of the 616 FSAM build. Vickers microhardness was measured on the cross section perpendicular to the WD of the FSAM sample using a load of 200 g and a holding time of 15 s. Microhardness tests were systematically performed along the centerlines of the sample in both transverse (TD) and normal (ND) directions, employing step sizes of 1 mm and 0.5 mm, respectively. The schematic diagram of the microhardness measurement path is provided in Fig. 2b.

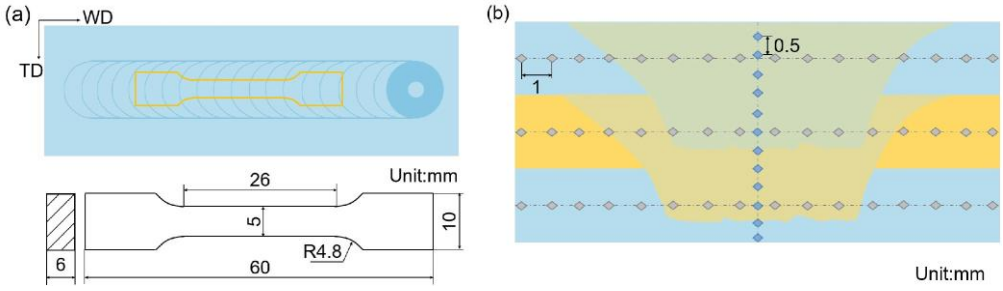


Fig. 2 Dimensions of tensile sample (a) and test path diagram for microhardness sample (b).

3. Results and Discussion

3.1 Materials mixing and flow features

Fig. 3 reveals the macro- and microstructural characteristics of the cross-sectional 616 FSAM build. As shown in Fig. 3a, the build contains three layers, within which two stir zones (SZ_1 and SZ_2) were formed. Additionally, no visible defects can be found at the bottoms of the SZs, suggesting the occurrence of adequate vertical material flow, which proves the appropriate selection of FSAM processing parameters. To further elucidate the material mixing and flow behavior within the SZs, representative regions (as marked in Fig. 3a) were examined at high magnification using optical microscopy. Owing to varying corrosion resistance among the dissimilar aluminium alloys, AA6061 and AA1100 alloys can be differentiated through their color contrast after chemical etching. AA6061 appears lighter, whereas AA1100 displays a darker contrast. Figs. 3b-3d show the optical micrographs of Regions 1, 2 and 3, corresponding to central regions of each additive layers, respectively. Pronounced material intermixing, characterized by banded structures and mechanical interlocking between dissimilar alloys, is evident in Regions 1 and 3 (Figs. 3b and 3d), respectively, suggesting effective thermal plasticization under the stirring action of the rotating tool. Besides, an onion ring flow pattern, accompanied by banded structures, is observed in Region 2 (Fig. 3c), which can be attributed to the strong stirring effect induced by the threaded pin, indicating enhanced material flow. The formation of banded structure, onion ring pattern and material interlocking confirm significant intermixing between dissimilar aluminum alloys in SZs of the 616 FSAM build. Furthermore, the microstructure of thermal mechanical affected zones below the SZs (Regions 4 and 5) were examined using SEM images in backscattered electron mode at higher magnification (see Figs. 3e and 3f). Clear interfacial bonding between AA6061 and AA1100 with an even distribution of fine precipitates in white and black colors on either side can be found in Region 4, as shown in Fig. 3e, verifying the appreciable intermixing of materials and the fragmentation of precipitates. Moreover, fine equiaxed grains are formed in Region 4, which is attributed to the occurrence of dynamic recovery and dynamic recrystallization under the action of tool pin [25-27]. Interestingly, the refinement of grains is also discovered in Region 5, with a significant reduction in grain size compared to base metal, as revealed in Figs. 3f and 3g. This finding aligns with our previous work [28], and the underlying mechanism has been discussed. When tool tilt angle is set as 0°, Region 5 receives strain rate and temperature originated from

thermal mechanical effect of pin tip, probably promoting recovery and recrystallization, which results in the formation of fine grains. Additionally, there are some large-sized precipitates distributing in Region 5, differing noticeably from Region 4. This can be attributed to the fact that the plastic deformation induced by tool pin tip in Region 5 was insufficient to fracture the precipitates during manufacturing. To further explore microstructure evolution along the build depth for the 616 FSAM build, EBSD analysis are performed at aforementioned regions. More detailed information on the crystallographic characteristics and texture features are elaborated in the following sections.

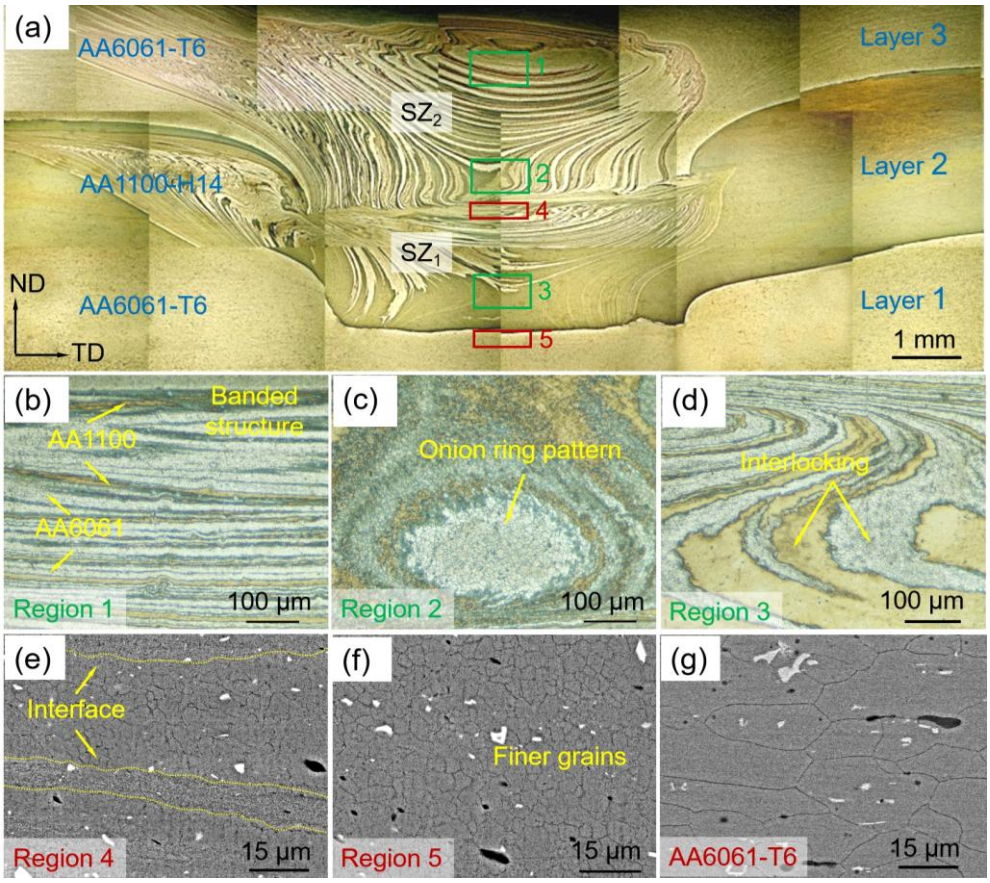


Fig. 3 Cross section macro structure of the 616 FSAM build (a) and microstructure of selected regions, including Region 1 (b), Region 2 (c), Region 3 (d), Region 4 (e), Region 5 (f) and as-received AA6061-T6 base metal (g).

3.2 Crystallographic characteristics

3.2.1 Base metals

Figs. 4a and 4b show the IPF maps of AA6061-T6 and AA1100-H14 alloys, respectively. Their grains present coarse and elongated features with average grain sizes of 25.5 μm and 25.8 μm, as revealed in grain size distribution maps (Figs. 4c and 4f), which are expected for conventionally rolled aluminum alloys. In addition, the misorientation angle distribution maps

for AA6061-T6 and AA1100-H14 alloys are indicated in Figs. 4b and 4e, respectively. The fractions of low-angle grain boundaries (LAGBs, misorientation range: 2°-15°) and high-angle grain boundaries (HAGBs, misorientation>15°) are statistically analyzed. A higher fraction of HAGBs can be noted in AA1100-H14 alloy, which may be associated with higher strain deformation imposed on this alloy during fabrication. Besides, the misorientation distribution corresponding to AA6061-T6 and AA1100-H14 alloys are obvious bimodal type, following random distribution.

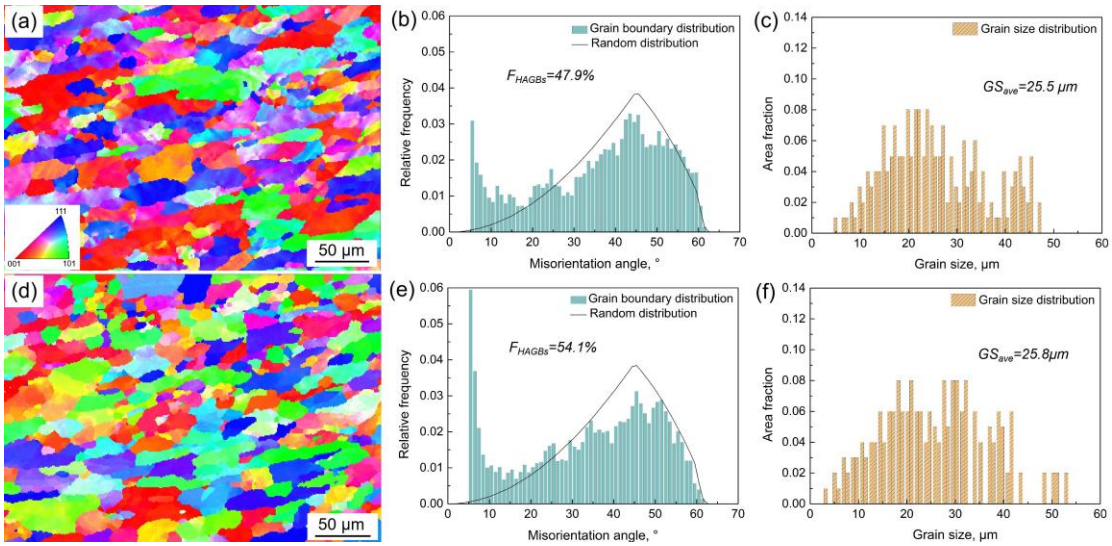


Fig. 4 IPF maps (a,d), corresponding misorientation angle distribution (b,e) and grain size distribution (c,f) for AA6061-T6 and AA1100-H14 aluminum alloys, respectively.

3.2.2 616 FSAM build

Due to the impact of thermal cycling time and plastic deformation degree, distinct crystallographic characteristics developed in various regions along the build depth. For the convenience of comparative analysis and description of the microstructure features in different regions from the top to the bottom of the build, subsequent discussions will focus on the central regions of each layer (Regions 1, 2, and 3) and thermal mechanical affected zones below the SZs (Regions 4 and 5).

Fig. 5 presents the EBSD results obtained from Regions 1-5. The inverse pole figure (IPF) maps corresponding to Regions 1, 2 and 3 (Figs. $5a_1$-$5c_1$) reveal that grain orientations in Regions 2 and 3 appear random related to appropriate flow and intermixing of materials during FSAM. In contrast, Region 1 exhibits a dominant green contrast, corresponding to a strong <101> preferred orientation. This orientation development is attributed to the higher degree of compressive and shear deformation induced by both the tool shoulder and pin in

Region 1, compared with Regions 2 and 3 [29,30]. Similarly, the IPF maps for Regions 4 and 5 (Figs. $5d_1$ and $5e_1$) also exhibit a <101> preferred orientation, which is associated with shear deformation introduced by the pin tip, especially under the tool tilt angle of 0°. Additionally, white and black lines marked in Figs. $5a_1$-$5e_1$ are utilized to denote LAGBs (Misorientation of 2°-15°) and HAGBs (Misorientation>15°), respectively. The quantified grain boundary fractions for each region are summarized in the histogram in Fig. $5f_1$. Notably, all regions exhibit a higher fraction of HAGBs, which is also identified in some previous studies [31-34].

Figs. $5a_2$-$5e_2$ illustrate the recrystallized, substructured, and deformed grain distribution maps for Regions 1-5, derived from internal average misorientation (IAM) values of individual grains. Recrystallized grains (IAM<1°), substructured grains (grains with IAM < 1° but inter-subgrain misorientation > 1°), and deformed grains (IAM>1°) are color-coded in blue, yellow and red, respectively. The corresponding recrystallized fractions for each region are shown in Figs. $5f_2$. The presence of a higher fraction of substructured grains can be noticed in each region, suggesting the dominance of dynamic recovery mechanism. Combined with the optical metallographic analysis (refers to Fig. 3), it is evident that Region 3 is mainly composed of AA1100 aluminum. Due to its high stacking fault energy, pure Al facilitates dislocation motion via cross-slip and climb, leading to dynamic recovery as the dominant softening mechanism under thermal deformation [35]. Hence, high degree of dynamic recovery occurred in Region 3, upon undergoing single plastic deformation and twice thermal cycles during FSAM. Numerous substructured grains are generated in Region 3, with the substructured fraction reaching 77.3%, as revealed in Figs. $5c_2$ and $5f_2$. The average grain size of Region 3 is 10.5±5.3 μm, which is apparently larger than those in Region 2 (4.9±2.8 μm) and Region 1 (6.5±4.2 μm), as indicated in Fig. $5f_1$. This coarsening behavior is mainly attributed to the absence of solute drag effects in AA1100, which allows unhindered dislocation movement and promotes grain growth. However, a high percentage of HAGBs exists in Region 3, rather than LAGBs being predominant (see Fig. $5f_1$). Combined with IPFs in Figs. $5a_1$-$5e_1$, adjacent substructured grains with visible color gradient can be observed, depicted by yellow circles, proving continuous rotation of orientation in these regions. The same result is predicted by Prangnell et al. [36], who reported that shear strain applied by stir tool drives the rotation and coalescence of subgrains, accumulating grain boundaries

misorientation more than 15°, which induces the formation of HAGBs. For Region 2, the content of AA6061 aluminum alloy enhances after undergoing twice stirring and mixing. The existence of hard base metal is conductive to increase strain rate, contributing to recrystallization, as shown in Figs. $5b_2$ and $5f_2$, which leads to grain refinement in Region 2. The proportion of recrystallized grains in Region 1 rise further to 39.5% (see Figs. $5a_2$ and $5f_2$), exhibiting higher degree of recrystallization, due to more intense plastic deformation imposed by tool shoulder. Despite this, the fraction of HAGBs in Region 1 decreases instead of increasing, as depicted in Fig. $5f_1$, which may be attributed to subgrain rotation. Owing to closer proximity between Region 1 and tool shoulder, high strain rate was generated, being a driving force for dislocation multiplication in Region 1. Although these dislocations are annihilated once exposed to elevated temperature, LAGBs cannot be fully transformed into HAGBs, ascribed to rapid heat dissipation in Region 1, inducing a decline in HAGBs fraction [37]. In addition, the larger average grain size in Region 1 compared to Region 2 (Fig. $5f_1$) is likely due to elevated frictional heat in proximity to the tool shoulder, promoting grain coarsening.

The fraction of substructured grains in Region 4 increases to 83.3%, as indicated in Figs. $5d_2$ and $5f_2$, after undergoing two thermoplastic deformations, implying higher degree of dynamic recovery. The high percentage of HAGBs (63.6%) in Region 4 is attributed to subgrains rotation and coalescence under shear action of tool pin. For Region 5, the substructured proportion enhances to 98.3% (see Figs. $5e_2$ and $5f_2$), presenting the occurrence of greater recovery during secondary thermal cycle. The average grain sizes in Regions 4 and 5 are 2.7±1.7 μm and 2.6±1.8 μm, respectively, as revealed in Fig. $5f_1$. Compared to Regions 1-3, finer grains are formed in Regions 4 and 5, owing to lower frictional heat produced by pin tip, preventing the grain growth. Overall, different regions within the 616 FSAM build are all governed by the subgrain refinement mechanism, resulting in a fine equiaxed grain structure.

To investigate the dislocation density evolution in distinct regions of the 616 FSAM build, the kernel average misorientation (KAM) maps were extracted from the EBSD datasets, as shown in Figs. 6a-6e. The average KAM values were computed using analysis software for Regions 1-5, corresponding to 0.61°, 0.59°, 0.63°, 0.45° and 0.46°, respectively, as displayed

in Fig. 6f. There is a minor fluctuation in KAM values among Regions 1, 2 and 3, while Region 3 exhibits a higher KAM value compared to Regions 1 and 2, indicating more dislocations existing in Region 3. In addition, the local misorientation in Region 4 is close to that in Region 5, implying that these two regions contain similar dislocation density. For clarifying the quantitative distribution of dislocation density, the density of geometrically necessary dislocation (ρ^{GND}) in Regions 1-5 was calculated using the following mathematical equation [38]:

$$\rho^{GND} = \frac{2KAM_{ave}}{\mu b} \tag{1}$$

where KAM_{ave} represents the average local misorientation of the selected regions, μ is the EBSD scanning step size (0.5 μm for Regions 1-3 and 0.15 μm for Regions 4-5), and b is the Burgers vector of aluminium alloy (0.286 nm). The ρ^{GND} values of Regions 1-5 are calculated and illustrated in Fig. 6f. It can be seen that the ρ^{GND} of Regions 1, 2 and 3 are 1.49×10^{14} m^{-2}, 1.44×10^{14} m^{-2} and 1.54×10^{14} m^{-2}, respectively. As expected, Region 3 possesses the maximum ρ^{GND} among Regions 1-3, which correlates well with the previously discussed recrystallization behavior. A higher ratio of substructured grains occupied Region 3 after undergoing twice thermal cycles, leading to a rise in dislocation density. Notably, the ρ^{GND} values of Regions 4 and 5 calculated by Eq. (1) are 3.66×10^{14} m^{-2} and 3.74×10^{14} m^{-2}, respectively, which increase significantly compared to those of Regions 1-3. During FSAM, strong strain gradient appeared surrounding tool pin, numerous GNDs were necessitated to generate at thermal mechanical affected zones below the SZs to coordinate inhomogeneous plastic deformation, inducing an increase in ρ^{GND} of Regions 4 and 5.

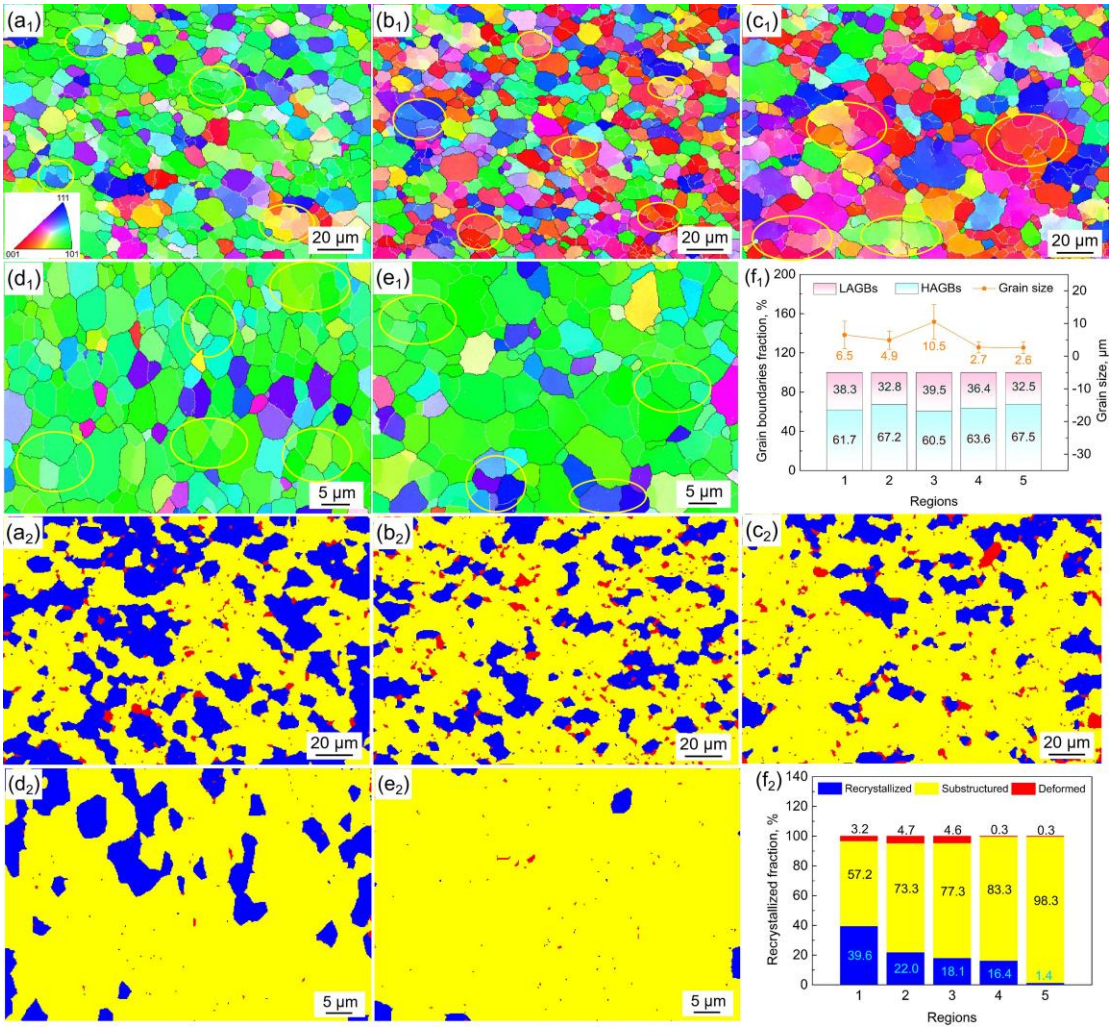


Fig. 5 IPF maps of Regions 1-5 (a_1-e_1), grain boundaries fractions and average grain size of different regions (f_1), distribution maps of recrystallized, substructured and deformed grains at Regions 1-5 (a_2-e_2), recrystallized fractions of different regions (f_2).

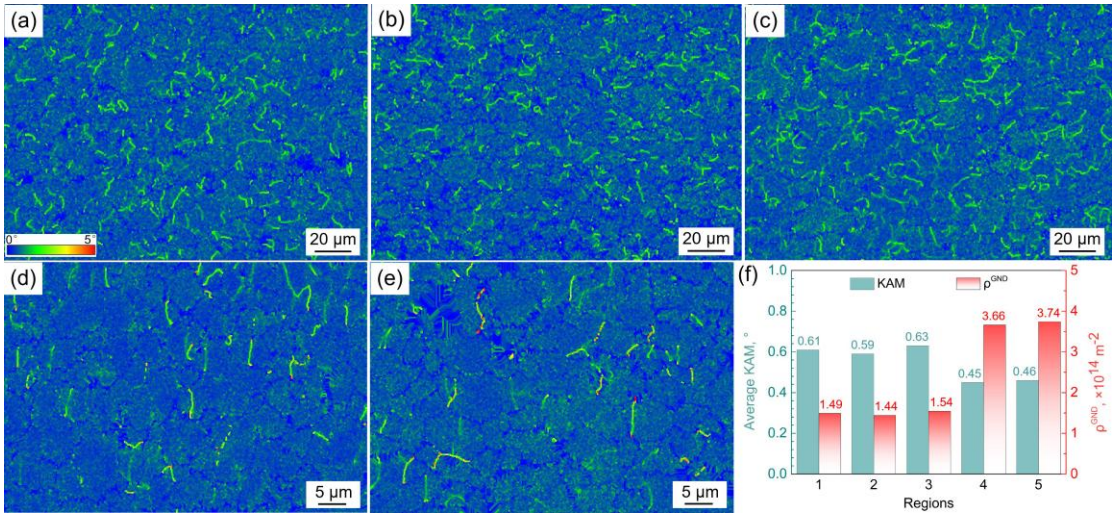


Fig. 6 KAM maps of Regions 1-5 (a-e) and statistical diagram containing average KAM and ρ^{GND} of different regions (f).

3.3 Texture features of the 616 FSAM build

During the FSAM process, intense plastic deformation subjected to SZs of the build causes the generation and evolution of various textures. The texture features of specific regions within the 616 FSAM build were analyzed via pole figures (PFs) and orientation distribution function (ODF) diagrams at three Euler angles (0°, 45°, 65°). The textures are labeled as {hkl}<uvω>, where {hkl} is the crystallographic plane perpendicular to the ND, and <uvω> is the crystallographic direction parallel to the TD, considering the rotational action of the tool.

Fig. 7 reveals (100), (110) and (111) PFs of Regions 1-5. All PFs exhibit pronounced asymmetry, which is attributed to significant plastic deformation imposed during the FSAM process [39]. Moreover, compare to Regions 1-3, stronger textures are formed at Regions 4 and 5, with maximum intensities of 11.45 and 12.76, respectively. The obtained ODF diagrams of Regions 1-5 are depicted in Figs. 8a-8e, respectively, and the texture components can be identified according to the corresponding ideal positioning schematics of textures for FCC materials [40-42], as indicated in Fig. 8f. Quantitative texture component fractions were calculated and are summarized in Tables 2 and 3. Clearly, Region 3 predominantly consists of S {123}<634>, Brass {110}<112> and Goss {011}<100> deformed textures, owing to the intense plastic deformation induced by tool pin. The S orientation exhibits the highest proportion at 18.8%, as summarized in Table 2. Additionally, some minor $Cube_{RD}$ {013}<100> recrystallized texture and A {112}<011> shear texture can also be observed in this region, as shown in Fig. 8c. Due to repeated thermal cycles, recovery and nucleation happened in the deformed substructure with cubically orientation. The subsequent recrystallization and grain growth processes evolved into the Cube {001}<100> texture by consuming adjacent substructures with non-cubic orientations [43]. However, due to the major existence of soft 1100 Al in Region 3 inducing comparatively weak shear strain, the deflection of Cube {001}<100> texture was actuated to form $Cube_{RD}$ {013}<100> texture [44]. For Region 2 (Fig. 8b), strong Goss {011}<100>, S {123}<634> deformed textures and Rt Cube {001}<110> shear texture with a peak intensity of 5.88, weak Brass {110}<112> deformed texture, $Cube_{RD}$ {013}<100>, $Cube_{ND}$ {001}<310> and P {011}<122> recrystallized textures are observed. Compared to Region 3, the intensity of deformed and

shear texture components increase greatly in Region 2, ascribed to experiencing twice severe plastic deformation. Besides, the total fraction of recrystallized textures including $Cube_{RD}$, $Cube_{ND}$ and P is enhanced, as detailed in Table 2, which is attributed to higher degree of recrystallization in Region 2. From Fig. 8a, it is noted that C {110}<110> with a peak intensity of 8.56 and A {112}<011> shear textures, P {011}<122> recrystallized texture, as well as Brass {110}<112> deformed texture prevail in Region 1. The major presence of A and C orientations confirms the availability of adequate shear strain suffering from tool shoulder in the Region 1. However, the intensity of P recrystallized texture decreases significantly, which may be influenced by discontinuous dynamic recrystallization mechanism [39]. Regions 4 and 5 exhibit similar texture characteristics, evolving into more prominent C {110}<110> and A {112}<011> shear textures with small amounts of Rt Cube {001}<110> and B/$\overline{B}$ {111}<110> components, as displayed in Figs. 8d and 8e, under the shear action of pin tip. Moreover, an appreciable presence of P recrystallized texture can be seen in Region 4, showing that the combined heat input and strain accumulated in this region are sufficient to obtain major P orientation. The volume fraction of C orientation is the highest and in excess of 37% in both Region 4 and Region 5, as detailed in Table 3. In addition, a noticeable rise in intensity of C texture can be found, implying full rotation of crystal lattices under the shear action of pin tip. In summarize, although the FSAM build exhibits the variation in texture evolution along the build depth, shear and deformed textures serving as major component form in all selected regions owing to its thermo-mechanical effect, which aligns with the results reported by some previous studies [40,45].

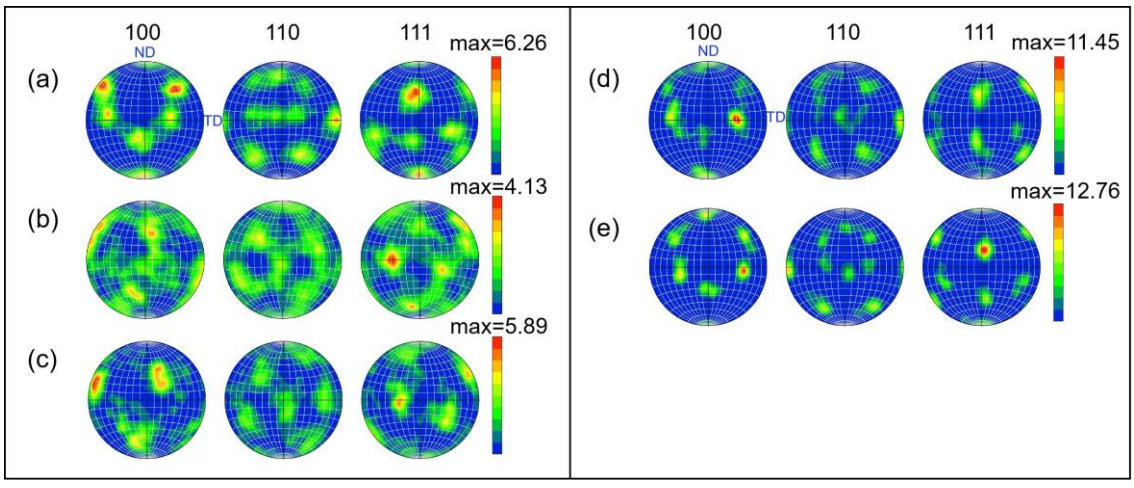


Fig. 7 The (100), (110) and (111) PFs of Regions 1-3 (a-c) and Regions 4-5 (d-e).

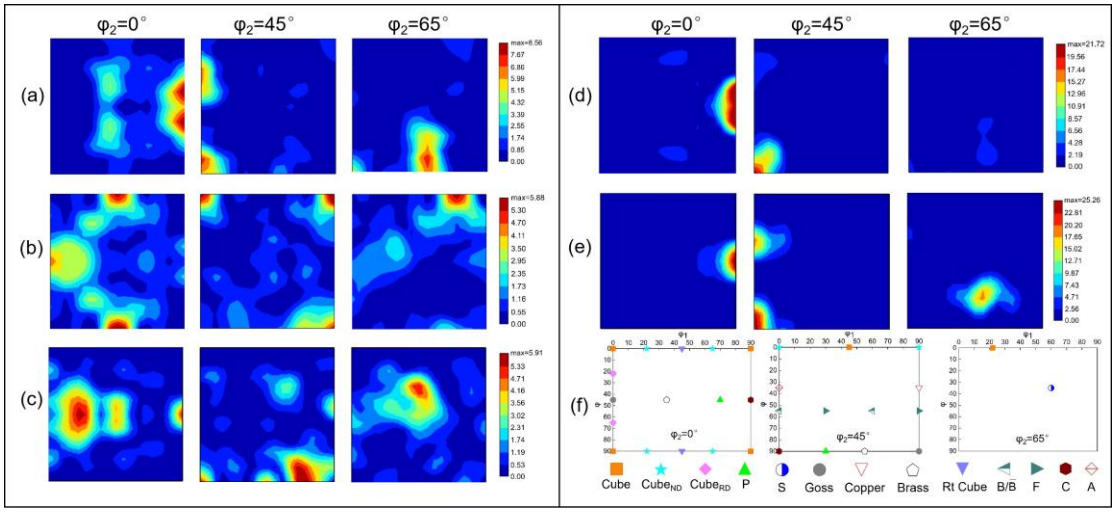


Fig. 8 The ODF diagrams of Regions 1-3 (a-c), Regions 4-5 (d-e) and at Euler angles of 0°, 45° and 65° and the ideal positioning of ODF texture components for FCC materials (f) at φ=0°, 45°and 65° sections.

Table 2 The volume fractions of texture components at Regions 1-3.

Texture types	Miller indices {hkl}<uvw>	Volume fraction, %		
		Region 1	Region 2	Region 3
Recrystallization	Cube {001}<100>	0.6	0.5	0.5
	$Cube_{ND}$ {001}<310>	1.7	8.4	10.1
	$Cube_{RD}$ {013}<100>	3.2	7.9	1.7
	P {011}<566>	11.2	7.3	5.6
	S {123}<634>	4.9	10.3	18.8
Deformation	Goss {011}<100>	--	13.2	11.6
	Copper {112}<111>	1.1	5.2	4.2
	Brass {110}<112>	11.0	8.5	15.4
	Rt Cube {001}<110>	5.5	11.0	2.3
	$B/\overline{B}$ {111}<110>	3.7	3.9	4.2
Shear	F {111}<112>	--	4.5	1.9
	C {110}<110>	19.1	3.3	2.8
	A {112}<011>	23.0	2.1	7.1

Table 3 The volume fractions of texture components at Regions 4 and 5.

Texture types	Miller indices {hkl}<uvw>	Volume fraction, %	
		Region 4	Region 5
Recrystallization	Cube {001}<100>	--	--
	$Cube_{ND}$ {001}<310>	--	--
	$Cube_{RD}$ {013}<100>	1.5	--
Deformation	P {011}<566>	21.4	7.9
	S {123}<634>	1.9	2.4
	Goss {011}<100>	--	--
	Copper {112}<111>	0.6	2.7
	Brass {110}<112>	--	1.1
	Rt Cube {001}<110>	8.8	--
Shear	$B/\overline{B}$ {111}<110>	7.7	5.4
	F {111}<112>	--	3.1
	C {110}<110>	37.0	37.5
	A {112}<011>	11.6	34.5

3.4 Morphology of precipitates at stir zones

Based on the SEM images depicted in Fig. 3, there were distinct differences in the size and distribution of precipitates between FSAM sample and AA6061-T6 base metal. Owing to the stirring action of tool pin during FSAM, continuously distributed precipitates in the base metal were fragmented into finer and dispersed particles in the SZs. Additionally, the heat input at SZs during FSAM was an important factor affecting the type and dissolution of precipitates, particularly for precipitate-strengthened aluminum alloys. The morphology and composition of precipitates at SZs of the 616 FSAM build were investigated using TEM analysis, and the results are shown in Fig. 9. Combined with the selected area electron diffraction (SAED) technique, the presence of Al_8Fe_2Si and Mg_2Si (β) precipitates in micron

scale can be noticed at SZs after FSAM, as shown in Figs. 9a and 9b. In addition, some coarse rod-shaped Mg_9Si_5 (β') precipitates are also found in SZs, confirmed by high-resolution TEM (HRTEM) and the corresponding fast Fourier transformation (FFT) image, as revealed in Figs. 9c and 9d. Meanwhile, the gray spot-like features are identified as cross-sections of the rod-shaped β' phase. However, acicular Mg_5Si_6 (β") precipitate that normally develops in AA6061-T6 aluminum alloy, is not observed in the SZs. To understand the phase transformation behavior within SZs, the peak temperature (T) during manufacturing is estimated using the following equation [46]:

$$\frac{T}{T_m} = K\left(\frac{\omega^2}{v \times 10^4}\right)^{\alpha} \tag{2}$$

where ω is rotation speed (1100 r/min) and ν is traverse speed (120 mm/s) of the stir tool, the values of constant K and exponent α are 0.65-0.75 and 0.04-0.05, respectively, while T_m is the melting temperature of base metal (933 K). After calculation, the peak temperature within SZs during FSAM ranges from 607 K to 700 K, which is higher than the dissolution temperatures of β" and β' precipitates (558 K and 653 K) [47,48]. Thus, the complete dissolution of β" precipitate and obvious coarsening of β' and β precipitates are occurred during FSAM thermal cycles. To sum up, the main precipitates presented in SZs are Al_8Fe_2Si, β and β'.

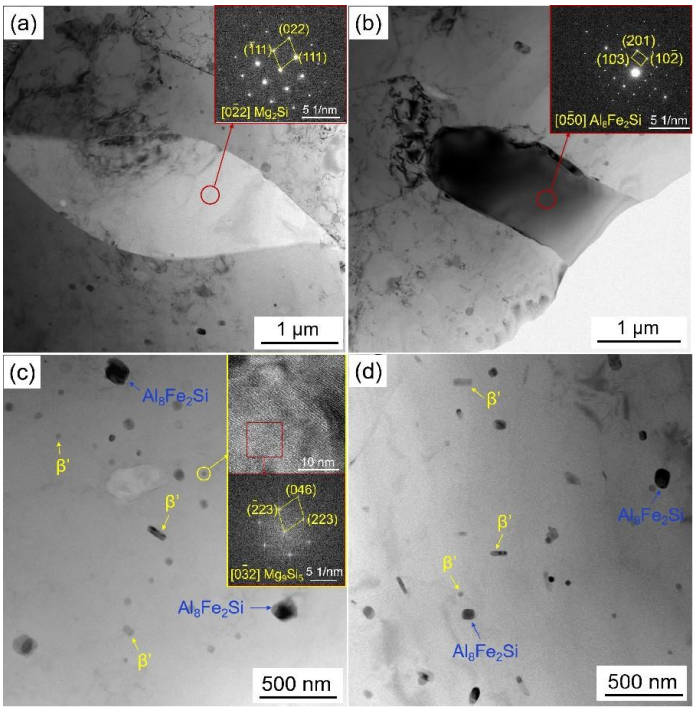


Fig. 9 TEM images and corresponding SAED patterns of precipitates in micron scale (a), (b) and TEM micrographs of precipitates at center of SZ_1 (c) and SZ_2 (d).

3.5 Mechanical properties of the 616 FSAM build

3.5.1 Tensile properties

A comparative analysis on tensile properties between 616 FSAM build and base metals was conducted and the corresponding histograms of strength and elongation for tensile samples are presented in Fig. 10a. The measured date of these materials are listed in Table 4. The 616 FSAM sample exhibits a yield strength (YS) of 101.3 MPa and an ultimate tensile strength (UTS) of 213.0 MPa, which are significantly higher than those of the AA1100-H14 base metal (YS: 77.5 MPa, UTS: 161.5 MPa), yet approximately 40% lower than those of the AA6061-T6 base metal. However, the average elongation (EL) value of 616 FSAM sample reaches 21.7%, exceeding 30% of base metals. It is notable that the achieved tensile strength did not conform to the Hall-Petch relationship ($\sigma=\sigma_0+kd^{-1/2}$, where σ is the strength of material, σ_0 and k are the contents, d is the grain size) [39], which reflects a direct correlation between grain size and strength of material. Although the 616 FSAM sample composes of fine grains, the YS and UTS values are still falling. For precipitate-hardened alloys, such as AA6061-T6 alloy, the precipitates have a greater impact on material strength in comparison with grain size [49]. According to TEM results (see Fig. 9), the strengthening precipitate (β" and β' phases) undergoes dissolution and coarsening in the SZs owing to thermal exposure cycles during FSAM, which is prone to cause a drop in tensile strength. In addition to precipitate-hardened effects, crystallographic texture also plays a critical role in the mechanical performance of the FSAM build. To establish the relationship between texture features and tensile properties of the 616 FSAM sample, the Schmid factor (SF) along WD is statistically analyzed for each region and the corresponding SF distribution maps and statistics are shown in Figs. 10b-10f. Regions 1-5 exhibit high proportions of grains with SF values exceeding 0.4—accounting for 93.6%, 90.5%, 92.4%, 92.3% and 88%, respectively. In addition, the SF_{ave} values for all selected regions are greater than 0.45, indicating a major presence of soft orientated grains. This soft orientation distribution reduces the critical resolved shear stress required for slip, thereby lowering the overall yield strength of the 616 FSAM build [50].

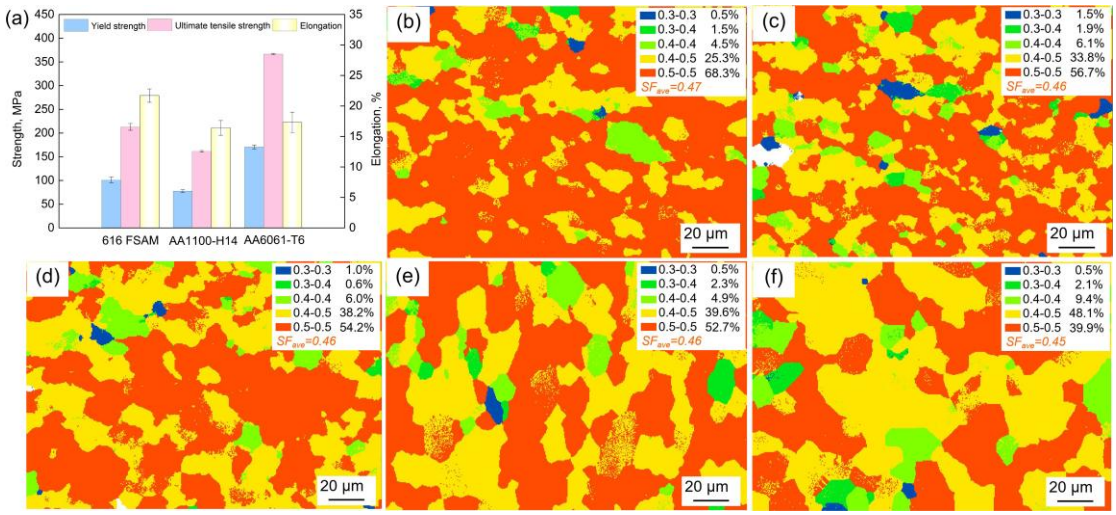


Fig. 10 Tensile properties of samples (a) and SF distribution maps of the Regions 1-5 (b-f).

Table 4 Tensile properties of AA6061-T6, AA1100-H14 base metals and 616 FSAM build along with standard deviation values.

Material	YS (MPa)	UTS (MPa)	EL (%)
AA6061-T6	170.5±4.4	365.4±1.7	17.3±1.7
AA1100-H14	77.5±2.3	161.5±1.8	16.4±1.1
616 FSAM	101.3±5.7	213.0±7.1	21.7±1.0

Fig. 11 presents the fracture morphology of the 616 FSAM sample. At low-magnification observation of the fracture surface in Fig. 11a, evident plastic deformation is noted, manifested as an uneven surface and evidence of necking, which are characteristics of ductile fracture. Besides, local areas near the bottom of the SZs (Fig. 11b) display mechanical sliding traces with a smooth surface morphology, implying the occurrence of interfacial debonding, which can be also proved by the shape and trend of engineering stress-strain curves of the 616 FSAM samples, as shown in Fig. 11c. A clear drop in stress can be seen after entering plastic deformation stage of the curve, which is significantly different from common aluminum alloys. During FSAM, the kissing bonding may be generated at interface of the build under the thermal and deformation conditions. Local interfacial debonding is prone to occur under relatively low applied stress, leading to the observed stress drop. Notably, these weakly bonded areas can undermine the overall tensile strength of the FSAM sample. In addition, stress serration behavior can be found for 616 FASM samples (see Fig. 11c), which is associated with the existence of finer grains. Some previous studies have reported that with the decrease of grain size, the stress serration increase [51,52]. Furthermore, Komarasamy et

al. [53] indicated that stress serration also depends on dislocation-dislocation interaction, grain boundary strengthening and dislocation particle interaction. At the initial stage of deformation, mobile dislocations diffuse with solute atoms, leading to the formation of dislocation loops around these particles. For plastic deformation to proceed, these dislocations must escape from this environment, requiring them to break away from the obstacles. This abrupt release of dislocations results in the formation of slip bands with higher displacement, which manifests as serrated flow in the stress-strain curve [54]. The higher dislocation storage and major presence of finer grains in 616 FSAM sample may be key contributors to the presence of stress serration during plastic deformation. Upon examination of the fracture surface at high-magnification in Fig. 11d, the ample presence of deep and coarse dimples along with internal serpentine sliding features can be noticed in central regions of each layer, indicative of a ductile failure mode, which leads to higher elongation of the sample. Additionally, fragmented precipitates are observed at the bottom of dimples, with coarse precipitates promoting the formation of larger dimples. The chemical compositions of these precipitates were also investigated using energy dispersion spectrum (EDS) analysis, and the results are illustrated in Figs. 11e and 11g. Accordingly, these coarse precipitates can be deduced as Al_8Fe_2Si and β phases, in line with the above-mentioned TEM results. Under tensile stress, the coarse precipitates and interface between matrix and precipitate tend to generate stress concentration. Subsequently, precipitates cracking and interfacial decohesion are prone to occur, leading to the formation of microvoids. These microvoids grow in size as the surrounding matrix undergoes plastic deformation. Ultimately, adjacent voids coalesce, leading to the formation of dimples and the final fracture. Fig. 11f indicates a high density of fine and shallow dimples combined with shear failure marks existing in thermal mechanical affected zone below the SZ, which is associated with fine grains generated in these regions. It is well-established that both dislocation mobility and void coalescence behavior are strongly grain size dependent [30]. Except for dimple features, thermal mechanical affected zones below the SZs exhibit shear failure marks, implying the ductile and shearing failure mode.

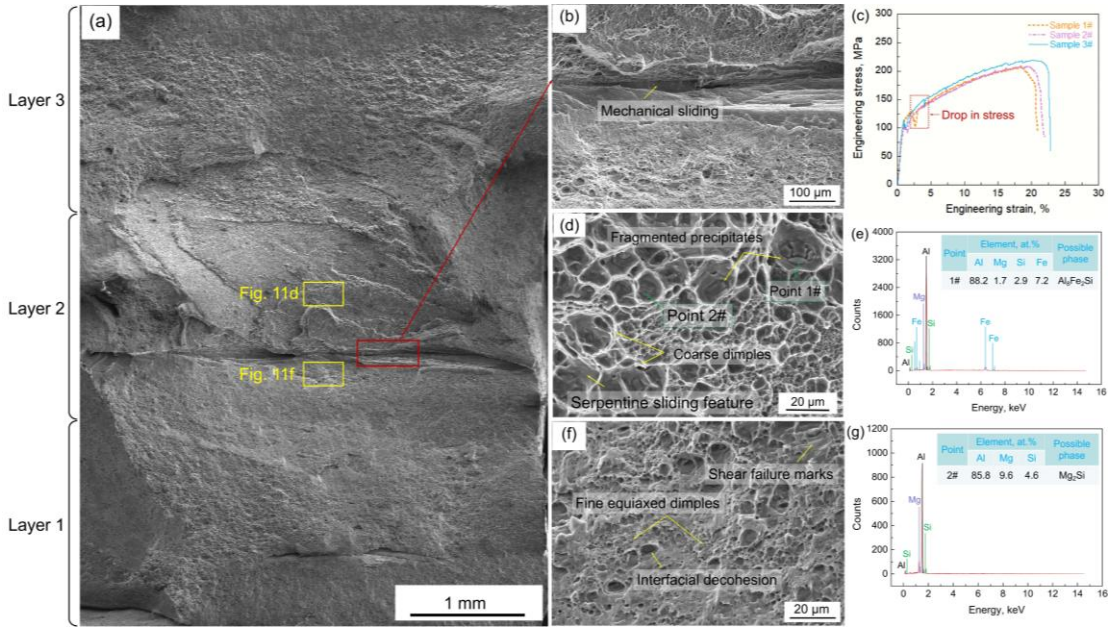


Fig. 11 Tensile fracture morphology of the 616 FSAM sample (a,b,d,f), engineering stress-strain curves for 616 FSAM samples (c) and EDS analysis results of Point 1# (e) and Point 2# (g) in Fig. 11d.

3.5.2 Microhardness distribution

Microhardness distribution of the 616 FSAM sample in the TD and ND on the cross-section are depicted in Figs. 12a and 12b, respectively. It can be seen from Fig. 12a that apart from Layer 2 (AA1100-H14), the central regions of Layers 1 and 3 possess the lower microhardness value compared to its base metal (AA6061-T6) along the TD. Despite fine-grained structure presenting in SZs, the dissolution and coarsening of precipitates occurred upon undergoing thermal cycles during FSAM, especially for AA6061-T6 alloy, leading to a significant decline in microhardness, which aligns with tensile results. Besides, the hardness distribution in central region of Layer 1 shows a fluctuating pattern. Conversely, the hardness distributions within the central regions of Layers 2 and 3 are relatively uniform, with similar average hardness values. This uniformity suggests effective and homogeneous material intermixing between AA1100-H14 and AA6061-T6 alloys. In addition, central region in Layer 2 contains higher hardness values than AA1100 base metal, which may be attributed to the presence of strengthening phases derived from AA6061-T6 alloy.

The hardness value of 616 FSAM sample appears an obvious descending trend along the build depth, as indicated in Fig. 12b. Small peaks in hardness occur at Regions 4 and 5 (denoted by red circles), and a higher degree of hardness rebound is evident in Region 5 relative to Region 4. EBSD results demonstrate that both regions underwent severe shear

deformation, generating elevated dislocation densities. Consequently, work hardening is identified as a key mechanism responsible for the hardness enhancement in these regions. Furthermore, combined with SF statistics (Fig. 10f), the SF_{ave} value in Region 5 is lower, indicating that more hard orientated grains are formed in this region, which has a positive influence on improving hardness of Region 5 [28].

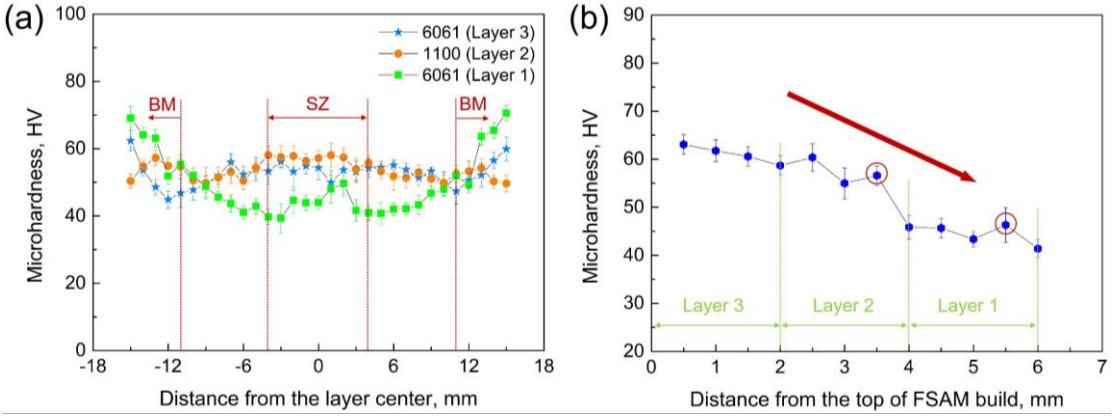


Fig. 12 Microhardness distribution along different directions of 616 FSAM build: (a) TD, (b) ND.

4. Conclusions

(1) The 616 FSAM build containing three dissimilar aluminum alloy layers was successfully produced with no significant defects at the bottom of SZs, confirming the adequate vertical material flow. The onion ring, banded structure and material interlocking features reveal significant intermixing between dissimilar aluminum alloys within the SZs.

(2) Due to the thermo-mechanical effect during FSAM, dynamic recovery and dynamic recrystallization occurred in the SZs. The central regions of each layer (Regions 1, 2 and 3) consist of fine equiaxed grains, with size ranging from 4.9 μm to10.5 μm. The average grain size of thermal mechanical affected zones beneath the SZs (Regions 4 and 5) were further decreased to below 3.0 μm. The fine equiaxed grain structure of 616 FSAM build was governed by the subgrain refinement mechanism. Additionally, the densities of geometrically necessary dislocation in Regions 4 and 5 were significantly higher than those in Regions 1-3.

(3) The 616 FSAM build exhibits the variation in texture evolution along the build depth owing to the changes in heat input and strain. Main deformed texture components (S {123}<634>, Goss {011}<100> and Brass {110}<112>) and the appreciable presence of shear textures (C {110}<110> and A {112}<011>) can be found in Regions 1-3. While grains in Regions 4 and 5 are mainly dominated by intense C {110}<110> and A {112}<011> shear

textures. The major precipitates retained in SZs are Al_8Fe_2Si, β and β'.

(4) The yield strength (101.3 MPa) and ultimate tensile strength (213.0 MPa) of 616 FSAM build along the WD are reduced to 60% of AA6061-T6 base metal owing to a major presence of soft orientated grains and the dissolution and coarsening of precipitates. Conversely, the total elongation of 616 FSAM build reaches 21.7%, increasing greatly compared to base metals.

Author Contribution declaration

Yuqiang Han: Writing-original draft, Conceptualization, Methodology, Investigation, Formal analysis, Visualization and Funding acquisition. Peifeng Wu: Investigation, Resources, Data Curation and Visualization. Chunfa Lin: Writing-review & editing, Conceptualization, Investigation, Supervision, Project administration and Funding acquisition. Sichang Zhang: Investigation, Validation, Data curation. Yaocheng Zhang: Writing-review & editing, Conceptualization, Resources and Supervision. Enhao Wang: Writing-review & editing, Supervision and Resources.

Declaration of Competing Interest

The authors declare that they have no known competing financial interests or personal relationships that could have appeared to influence the work reported in this paper.

Acknowledgements

The authors gratefully acknowledge the financial supports of this study by the Natural Science Research Project of Higher Education Institutions of Jiangsu Province (23KJ B430002) and Natural Science foundation of Jiangsu Province (BK20220690).

Data Availability

The raw/processed data required to reproduce these findings cannot be shared at this time due to legal or ethical reasons.

References

[1] Z. Zhu, Z. Hu, H.L. Seet, et al. Recent progress on the additive manufacturing of aluminum alloys and aluminum matrix composites: Microstructure, properties, and applications. International Journal of Machine Tools and Manufacture, 2023, 190:104047.

[2] X. Zhang, Y. Chen, J. Hu. Recent advances in the development of aerospace materials.

Progress in Aerospace Sciences, 2018, 97:22-34.

[3] T. Dursun, C. Soutis. Recent developments in advanced aircraft aluminium alloys. Materials and Design, 2014, 56:862-871.

[4] R. Montanari, A. Palombi, M. Richetta, et al. Additive manufacturing of aluminum alloys for aeronautic applications: advantages and problems. Metals, 2023, 13:716.

[5] S. Rathee, M. Srivastava, P.M. Pandey, et al. Metal additive manufacturing using friction stir engineering: A review on microstructural evolution, tooling and design strategies. CIRP Journal of Manufacturing Science and Technology, 2021, 35:560-588.

[6] Y. Wu, J. Fang, C. Wu, et al. Additively manufactured materials and structures: A state-of-the-art review on their mechanical characteristics and energy absorption. International Journal of Mechanical Sciences, 2023, 246:108102.

[7] Y. Geng, I. Panchenko, X. Chen, et al. Wire arc additive manufacturing Al-5.0 Mg alloy: microstructures and phase composition.Materials Characterization, 2022, 187:111875.

[8] W. Zhang, H. Yi, H. He, et al. Content effects of in-situ synthesis TiC for grain refinement, porosity suppression and performance enhancement in wire arc additive manufactured Al-Cu alloy. Journal of Materials Processing Technology, 2025, 340:118875.

[9] S.Z. Uddin, L.E. Murr, C.A. Terrazas, et al. Processing and characterization of crack-free aluminum 6061 using high temperature heating in laser powder bed fusion additive manufacturing. Additive Manufacturing, 2018, 22: 405-415.

[10] N. Li, T. Wang, L. Zhang, et al. Crack initiation mechanism of laser powder bed fusion additive manufactured Al-Zn-Mg-Cu alloy. Materials Characterization, 2023, 195:112415.

[11] Z. Tan, J. Li, Z. Zhang. Experimental and numerical studies on fabrication of nanoparticle reinforced aluminum matrix composites by friction stir additive manufacturing. Journal of Materials Research and Technology, 2021, 12(3):1898-1912.

[12] A. Das, T. Medhi, S. Kapil, et al. Multi-track multi-layer friction stir additive manufacturing of AA6061-T6 alloy. Progress in Additive Manufacturing, 2024, 9(4):835-855.

[13] K.K. Jha, R. Kesharwani, M. Imam. Microstructure and mechanical properties correlation of FSAM employed AA5083/AA7075 joints. Transactions of the Indian

Institute of Metals, 2022, 76(2):323-333.

[14] S. Olhan, B. Antil, B.K. Behera. Progress in metal additive manufacturing using innovative solid-state friction stir-based techniques. Journal of Alloys and Compounds, 2025, 1010:177395.

[15] S. Palanivel, R.S. Mishra. Building without melting: a short review of friction-based additive manufacturing techniques. International Journal of Additive and Subtractive Materials Manufacturing, 2017, 1(1):82-103.

[16] Y. Geng, M. Zhou, Y. Zhu, et al. Regulating microstructure of Mg-Li-Al-Zn alloy for enhancing comprehensive performance through friction stir additive manufacturing. Materials Science and Engineering A, 2024, 895:146239.

[17] A.K. Srivastava, N. Kumar, A.R. Dixit. Friction stir additive manufacturing-An innovative tool to enhance mechanical and microstructural properties. Materials Science and Engineering B, 2021, 263:114832.

[18] S. Palanivel, H. Sidhar, R.S. Mishra. Friction stir additive manufacturing: route to high structural performance. JOM, 2015, 67:616-621.

[19] S. Palanivel, P. Nelaturu, B. Glass, et al. Friction stir additive manufacturing for high structural performance through microstructural control in an Mg based WE43 alloy. Materials and Design, 2015, 65:934-952.

[20] Y. Mao, L. Ke, C. Huang, et al. Formation characteristic, microstructure, and mechanical performances of aluminum-based components by friction stir additive manufacturing. International Journal of Advanced Manufacturing Technology, 2016, 83:1637-1647.

[21] Z. Zhao, X. Yang, S. Li, et al. Interfacial bonding features of friction stir additive manufactured build for 2195-T8 aluminum-lithium alloy. Journal of Manufacturing Processes, 2019, 38:396-410.

[22] C. He, Y. Li, Z. Zhang, et al. Investigation on microstructural evolution and property variation along building direction in friction stir additive manufactured Al-Zn-Mg alloy. Materials Science and Engineering A, 2020, 777:139035.

[23] T. Jiang, T. Jiao, G. Dai, et al. Microstructure evolution and mechanical properties of 2060 Al-Li alloy via friction stir additive manufacturing. Journal of Alloys and Compounds, 2023, 935:168019.

[24] Y. Li, C. He, J. Wei, et al. Correlation of local microstructures and mechanical properties of Al-Zn-Mg-Cu alloy build fabricated via underwater friction stir additive manufacturing. Materials Science and Engineering A, 2021, 805:140590.

[25] M. Liu, B.Wang, X. An, et al. Friction stir additive manufacturing enabling scale-up of ultrafine-grained pure copper with superior mechanical properties. Materials Science and Engineering A, 2022, 857:144088.

[26] G.K. Padhy, C. Wu, S. Gao. Friction stir based welding and processing technologies-processes, parameters, microstructures and applications: A review. Journal of Materials Science and Technology, 2018, 34(1):1-38.

[27] M.R. Roodgari, R. Jamaati, H.J. Aval. Fabrication of a 2-layer laminated steel composite by friction stir additive manufacturing. Journal of Manufacturing Processes, 2020, 51:110- 121.

[28] Y. Han, K. Lv, C. Lin, et al. Sheet-based friction stir additive manufactured 6061 aluminium alloy:Microstructure, texture evolution and mechanical properties. Materials Science and Engineering A, 2024, 915:147295.

[29] L. Xing, L. Ke, C. Huang, et al. The formation mechanism of the friction stir welds. Materials Science and Technology Conference and Exhibition, 2009, 2586-2596.

[30] C. Zhang, G. Huang, Q. Liu. Quantitative analysis of grain structure and texture evolution of dissimilar AA2024/7075 joints manufactured by friction stir welding. Materials Today Communications, 2021, 26:101920.

[31] Q. Li, G. Huang, Y. Cao, et al. Microstructure refinement, strengthening and ductilization mechanisms in Al-Mg-Mn-Er-Zr alloy with high Mn content by friction stir processing. Materials Characterization, 2022, 189:111939.

[32] Y. Chen, H. Ding, S. Malopheyevz, et al. Influence of multi-pass friction stir processing on microstructure and mechanical properties of 7B04-O Al alloy. Transactions of Nonferrous Metals Society of China, 2017, 27(4):789-796.

[33] A. Kar, D. Yadav, S. Suwas,et al. Role of plastic deformation mechanisms during the microstructural evolution and intermetallics formation in dissimilar friction stir weld. Materials Characterization, 2020, 164:110371.

[34] J.Q. Su, T.W. Nelson, R. Mishra, et al. Microstructural investigation of friction stir

welded 7050-T651 aluminium. Acta Materialia, 2003, 51(3):713-729.

[35] H.J. McQueen, W. Blum. Dynamic recovery: sufficient mechanism in the hot deformation of Al (<99.99). Materials Science and Engineering A, 2009, 290(1-2):95-107.

[36] P.B. Prangnell, C.P. Heason. Grain structure formation during friction stir welding observed by the stop action technique. Acta Materialia, 2005, 53:3179-3192.

[37] X. Zeng, P. Xue, L. Wu, et al. Microstructural evolution of aluminum alloy during friction stir welding under different tool rotation rates and cooling conditions. Journal of Materials Science and Technology, 2019, 35:972-981.

[38] L.P Kubin, A. Mortensen. Geometrically necessary dislocations and strain-gradient plasticity: a few critical issues. Scripta Materialia, 2003, 48(2):119-125.

[39] A.S. Sundar, A. Kar, K.K. Mugada, et al. Enhancement of microstructure, micro-texture, and mechanical properties of Al6061 friction stir welds using the developed static shoulder welding tool. Materials Characterization, 2023, 203:113148.

[40] W. Tang, X. Yang, C. Tian, et al. Interfacial grain structure, texture and tensile behavior of multilayer deformation-based additively manufactured Al 6061 alloy. Materials Characterization, 2023, 196:112646.

[41] L. Su, C. Lu, A.A. Gazder, et al. Shear texture gradient in AA6061 aluminum alloy processed by accumulative roll bonding with high roll roughness. Journal of Alloys and Compounds, 2014, 594:12-22.

[42] K.K. Jha, M. Imam. Microstructure evolution and local mechanical properties of friction stir additively manufactured (FSAM) AA5083/AA6061/AA7075 gradient composite. Materials Science and Engineering A, 2024, 903:146668.

[43] M. Naseri, M. Alvand, E. Ahmadi, et al. Effect of cube texture on local softening of friction stir welded joints for nanostructured AA2024 processed by accumulative roll bonding. Journal of Materials Research and Technology, 2024,28:3507-3513.

[44] H. Jin, S. Saimoto, M. Ball, et al. Characterisation of microstructure and texture in friction stir welded joints of 5754 and 5182 aluminium alloy sheets. Materials Science and Technology, 2001, 17:1605-1614.

[45] Y. Li, G. Sun, Z. Zhang, et al. Texture evolution of refill friction stir spot welding in

alclad 2A12-T42 aluminum alloy. Materials Characterization, 2023, 205:113289.

[46] P. Agrawal, R.S. Haridas, P. Agrawal, et al. Deformation based additive manufacturing of a metastable high entropy alloy via Additive friction stir deposition. Additive Manufacturing, 2022, 60:103282.

[47] H.I. Dawood, K.S. Mohammed, A. Rahmatb, et al. Effect of small tool pin profiles on microstructures and mechanical properties of 6061 aluminum alloy by friction stir welding. Transactions of Nonferrous Metals Society of China, 2015, 25(9): 2856-2865.

[48] A. Ghosh, M. Ghosh, A.H. Seikh, et al. Phase transformation and dispersoid evolution for Al-Zn-Mg-Cu alloy containing Sn during homogenisation. Journal of Materials Research and Technology, 2020, 9(1):1-12.

[49] B. Chaudhary, N.K. Jain, J. Murugesan, et al. Friction stir powder additive manufacturing of Al 6061 alloy: Enhancing microstructure and mechanical properties by reducing thermal gradient. Journal of Materials Research and Technology, 2023, 26:1168-1184.

[50] C. Gu , X. Yang, W. Tang, et al. Effect of cube texture on local softening of stationary shoulder friction stir welding for thick-plate Al-Li alloy. Materials Letters, 2022, 324: 132724.

[51] S. P. Joshi, C. Eberl, B. Cao, et al. On the occurrence of portevin-Le châtelier instabilities in ultrafine-grained 5083 aluminum alloys. Experimental Mechanics, 2009, 49:207-218.

[52] S. Xia, M. Ma, J. Zhang, et al. Effect of heating rate on the microstructure, texture and tensile properties of continuous cast AA5083 aluminum alloy. Materials Science and Engineering A, 2014, 609:168-176.

[53] M. Komarasamy, R.S. Mishra. Serration behavior and shear band characteristics during tensile deformation of an ultrafine-grained 5024 Al alloy. Materials Science and Engineering A, 2014, 616:189-195.

[54] H. Halim, D.S. Wilkinson, M. Niewczas. The portevin-Le chatelier (PLC) effect and shear band formation in an AA5754 alloy. Acta Materialia, 2007, 55(12):4151-4160.